# Photopolarimetry Analysis of the Venus Atmosphere in Polar Regions

MAKOTO SATO

*NASA Goddard Institute for Space Studies/SSAI, 2880 Broadway, New York, New York 10025*
*E-mail: pdmrs@giss.nasa.gov*

LARRY D. TRAVIS

*NASA Goddard Institute for Space Studies, 2880 Broadway, New York, New York 10025*

AND

KIYOSHI KAWABATA

*Department of Physics, Science University of Tokyo, 1-3 Kagurazaka, Shinjuku-ku, Tokyo, Japan 162*

An analysis of linear polarization in the north and south polar regions of Venus observed by the Pioneer Venus orbiter during the first 2820 days of its mission has been performed to find microphysical properties of the submicrometer particles and to investigate the temporal variation of the optical thickness of the haze layer. The search for the best values of the physical properties and vertical distribution of the haze particles is based on minimization of the RMS discrepancy between the computed theoretical polarization and observed polarization, under the assumption that the variation of the observed polarization is due to the temporal variation of the optical thickness of the haze layer. This approach allows us to use a simple model which can explain well general features of the angular distribution of polarization for a large number of maps at wavelengths 935, 550, and 365 nm. We find that in the north polar region the haze particles have effective radius 0.25 ± 0.05 μm, effective variance 0.25 ± 0.05, and real part of the refractive index 1.435 ± 0.02 at wavelength 550 nm. In the south polar region, the haze particles have effective radius 0.29 ± 0.02 μm, effective variance 0.25 ± 0.03, and real part of the refractive index 1.45 ± 0.02 at wavelength 550 nm. Temporal variations of optical thickness of the haze particles in both polar regions seem to exhibit short-period quasi-oscillation features and our present analysis suggests some correlation between the variation in optical thickness of the haze layer in the north and south polar regions.  © 1996 Academic Press, Inc.

## 1. INTRODUCTION

To the remote observer of Venus, the dominant feature is the unbroken cloud layer shielding the planet's surface in visible light. Until the late 1960s, very little was known about the physical properties and vertical structure of these clouds. Then in the early 1970s several important studies revealed the microphysical properties of the cloud particles (Hansen and Arking 1971, Hansen and Hovenier 1974) through the analysis of ground-based polarimetry observations by Dollfus (1966), Coffeen and Gehrels (1969), and Dollfus and Coffeen (1970). At about the same time, analysis of spectrophotometry of Venus (Martonchik 1974, Samuelson *et al.* 1975, Young 1974, 1975) and physical chemistry studies (Sill 1972, Young 1973) strongly suggested that the chemical composition of the cloud particles was concentrated sulfuric acid. Early evidence regarding vertical structure at the top of the Venus clouds was provided by observations of the extension of the cusps of Venus in crescent phase and from its transits across the Sun (Dollfus and Maurice 1965, Goody 1967, Link 1969), which indicated a rather diffuse distribution. High altitude haze layers were apparent in the limb pictures taken by the Mariner 10 spacecraft (O'Leary 1975), in which two distinct layers separated by a few kilometers in altitude were observed. Martonchik and Beer (1975) invoked a haze layer lying above the main cloud and consisting of particles with radius 0.4 μm and optical thickness ~0.2 to explain the observed phase-angle dependence of the Venus reflectance in the 3–4 μm spectral region. Although this result seemed to be inconsistent with the earlier polarimetry analysis at visible wavelengths, Lane (1979) found evidence suggesting the existence of haze particles with radii on the order of 0.2 μm from spatially resolved Venus polarimetry obtained in 1975 (Gehrels *et al.* 1979).

Previous analysis of early data taken by the Pioneer Venus Orbiter Cloud Photopolarimeter (OCPP) revealed the existence of submicrometer particles extending above

TABLE I
Properties of Venus Clouds

| Region | Altitude (km) | Temperature (K) | Optical Depth ( at 630 nm) | Density (N cm$^{-3}$) | Particle Size (radius; $\mu$m) | Refractive Index |
|---|---|---|---|---|---|---|
| Upper Haze | 70.0 - 90.0 | 225 - 190 | 0.2 - 1.0 | 500 | 0.2 | 1.45 |
| Upper Cloud | 56.5 - 70.0 | 286 - 225 | 6.0 -8.0 | 1500<br>50 | 0.2 (mode 1)<br>1.0 (mode 2) | 1.44 |
| Middle Cloud | 50.5 - 56.5 | 345 - 286 | 10.0 - 12.0 | 300<br>50<br>10 | 0.15(mode 1)<br>1.25(mode 2)<br>3.5  (mode 3) | 1.42, 1.38 |
| Lower Cloud | 47.5 - 50.5 | 367 - 345 | 6.0 - 12.0 | 1200<br>50<br>50 | 0.2 (mode 1)<br>1.0 (mode 2)<br>4.0 (mode 3) | 1.32 (?) |
| Pre-cloud Layers | 47.5<br>46.0 | 367<br>378 | 0.1<br>0.05 | 150<br>50 | 0.15(mode 1)<br>1.0  (mode 2) | 1.46, 1.50 |
| Lower Haze | 31.0 - 47.5 | 482 - 367 | 0.1 - 0.2 | 20 | 0.1 | unknown |

the main cloud, with the polar regions typically exhibiting amounts of such haze greater than that observed at lower latitudes. Kawabata *et al.* (1980, hereafter referred to as Paper 1) estimated the haze particles to have effective radius $r_{eff} = 0.23 \pm 0.04$ $\mu$m, effective variance of the size distribution $v_{eff} = 0.18 \pm 0.1$, and real part of the refractive index $n_r = 1.45 \pm 0.04$. The average optical thickness of the haze layer in the polar region was found to be 0.83 at $\lambda = 365$ nm.

Beginning in the late 1970s, *in situ* measurements by the Venera 9–12 landers, the Pioneer Venus probes, and the Vega 1–2 balloon landers provided detailed information on the vertical structure and particle sizes below the cloud top (65 km altitude) region (Marov *et al.* 1977, Marov 1978, 1979, Marov *et al.* 1980, Knollenberg and Hunten 1980, Ragent and Blamont 1980, Sagdeev and Moroz 1986). Table I summarizes the Venus cloud and haze properties deduced from these Pioneer Venus, Venera, and Vega mission results (cf. Esposito *et al.* 1983). While the identification of the haze particles and most of the cloud particles as concentrated sulfuric acid seems relatively firm, there remains uncertainty regarding the source of near-ultraviolet absorption within the cloud and other "minor" chemical constituents (Krasnopolsky 1985, Hartley *et al.* 1989, Bezard *et al.* 1990, Carlson *et al.* 1991). Uncertainty also persists with respect to the phase and composition of the larger, mode 3 particles (Knollenberg and Hunten 1980, Andreichikov *et al.* 1987, Carlson *et al.* 1993, Grinspoon *et al.* 1993, Krasnopolsky and Pollack 1994).

In Paper 1, we deduced the properties of the haze based upon the analysis of OCPP polarimetry data obtained only during the nominal mission, *viz.*, the first 243 orbits. The longer-term OCPP data set permits us to refine the earlier estimates and address the question of temporal variability of the haze. In the present analysis, we use OCPP polarime-

try maps that cover the period from the start of the mission through orbit 2820 and employ a simple haze-cloud model to fit these data with our initial emphasis on the retrieval of the haze properties in the polar regions. The following section describes the polarimetry observations and summarizes the polarimetry maps employed in the analysis. This is followed by a description of the modeling approach and the results of our analysis.

## 2. DATA

The OCPP instrument obtains spin-scan maps using a positionable telescope, which can provide look angles in the range from 0° to 145° from the direction of the spacecraft spin axis, whose nominal orientation is toward the South ecliptic pole. Since the spacecraft is near Venus, the phase angle varies slightly from one map element to another (Travis *et al.* 1979). We define mean phase angles for each map, taken to be the averages over measurable pixels in each zone (e.g., polar or equatorial) of the visible planet disk weighted by the intensity. Because of the near-polar orientation of the spacecraft orbit, obtaining full phase angle coverage requires observation over almost one half the Venus sidereal year (~112 days); so to the extent that we employ characteristics of polarization dependence on phase angle, some shorter term temporal variation is more difficult to identify. The OCPP instrument measures intensity, linear polarization degree, and the direction of polarization at four wavelengths: 270, 365, 550, and 935 nm. Since the orbital period of the spacecraft is approximately 24 hr (Colin 1979), the orbit number essentially equals the number of terrestrial days elapsed since December 4, 1978, the day of orbit insertion.

For the analysis of polarimetry data in the equatorial and both polar regions, we have selected more than 700

maps from the first 2820 days of the Orbiter mission. After that point, the power sharing strategy resulted in the exclusion of polarimetry maps with phase angles larger than 90°, so we have restricted coverage to the earlier period to maintain approximately uniform distribution of maps with phase angle. Most of the selected maps have telescope look angles close to 90°, at which comparable views of both southern and northern hemispheres were obtained. Since one of our ultimate objectives is to determine whether the physical properties of aerosols in the polar regions differ systematically from those at lower latitudes, we have divided the maps into latitude zones: the north and south polar regions are defined as the zones from 90°N to 70°N and from 70°S to 90°S. A comparable number of pixels in the equatorial region is obtained by defining that zone as latitudes 2°N to 2°S. The present study is focused on the polar regions because the larger slant paths of illumination and observation, as well as the generally greater haze thickness there, permit haze property retrievals that are rather insensitive to model assumptions regarding the underlying clouds. Figure 1 displays the linear polarization degree vs phase angle (hereafter referred to as P–P diagram) for these maps at 935, 550, and 365 nm separately for the north and south polar regions. Data at 270 nm were not included in this analysis because of the low signal-to-noise ratio.

As described in Paper 1, the distinctive feature of the submicrometer haze particles is the often large positive polarization at middle phase angles for 935 nm in contrast to the negative polarization corresponding to the 1-$\mu$m cloud particles. The panels for 935 nm in Fig. 1 illustrate this quite effectively with various maps showing a very broad scatter of points over the phase angles between ~30° and ~160°. The natural interpretation of this scatter is that to first order, it represents variation in the optical thickness of the haze overlying the cloud. At phase angles below about 30°, it is more difficult to distinguish the polarization signatures of the haze and cloud particles, so we exclude those maps in most of our analysis to retrieve haze characteristics.

Closer examination of the large scatter in polarization over the broad range of phase angles reveals that much of the variation is attributable to the long time span for the full data set and that maps acquired over shorter periods show a more systematic, "well-behaved" variation that suggests a grouping into families or branches. Figure 2 illustrates such a grouping with solid lines approximately connecting the points for the maps of Fig. 1 into branches labeled A through K, with the respective ranges of corresponding orbit numbers for each branch listed in Table II. The sequences of three values separated by slashes for number of maps in Table II correspond (left to right) to: (i) the number of maps that have both polar zones visible, (ii) the total number of maps actually used for the analyses, and (iii) the total number of maps available prior to de-

scribed exclusions and restrictions. Pairs of haze optical thickness at 935 nm are averages over the maps in categories (i) and (ii) based upon our analysis described below. Branch A includes some data from the nominal mission that were used in Paper 1. However, more than half of the data used in Paper 1 are omitted from the present analysis, since we imposed the following restrictions to obtain more accurate results: (i) The intensity of each pixel used must be ≥100 DN. (ii) Each zone should have at least three pixels above the intensity threshold. (iii) Each map should have an approximately comparable view of both the southern and northern hemispheres. (iv) Each map should have data at all three wavelengths employed in the complete analysis.

Among the various branches in Fig. 2, the 19 maps from orbit number 1700–1720 that make up branch I in the north polar region have peculiar features: a markedly lower polarization degree at 550 and 935 nm, and a very high polarization degree at 365 nm around phase angles 90° ~ 120°. In contrast, maps before orbit 1640 show similar features to those after orbit 1790. This seemingly anomalous behavior can be seen over a broad range of latitude zones, although departures of the polarization features in the southern hemisphere are not so obvious as in the north polar region. Qualitatively, these features might be explained by a virtual absence of haze and lower than normal cloud top altitude resulting in higher polarization at 365 nm from Rayleigh scattering. Since our strategy is to determine average haze particle properties using a simple model that allows for modest temporal variation in the optical thickness of the overlying haze, we elected to exclude these 19 maps from the most general analysis and will report the results of a specific investigation of this branch in a future paper. After the indicated exclusions and restrictions, we have available for the present analysis 327 maps for the north polar region and 234 maps for the south polar region. This set of maps provides good sampling of phase angles and time as illustrated by Figs. 1 and 2 and Table II.

## 3. THEORETICAL MODEL

The simplest model that can explain the detailed features of the polarization data obtained by the OCPP requires three layers: the base cloud, an overlying haze layer, and clear gas above the haze. The existence of submicrometer haze particles above 70 km altitude has been established by analyses of several types of remote sensing data (Martonchik and Beer 1975, Lane 1979, Lane and Opstbaum 1983, Paper 1), and the qualitative inference from the 935 nm OCPP data in Fig. 1 is that substantial amounts of polar haze have been present at various times throughout the first eight years of the Pioneer Venus Orbiter mission. Since photons emerging from the atmosphere after several
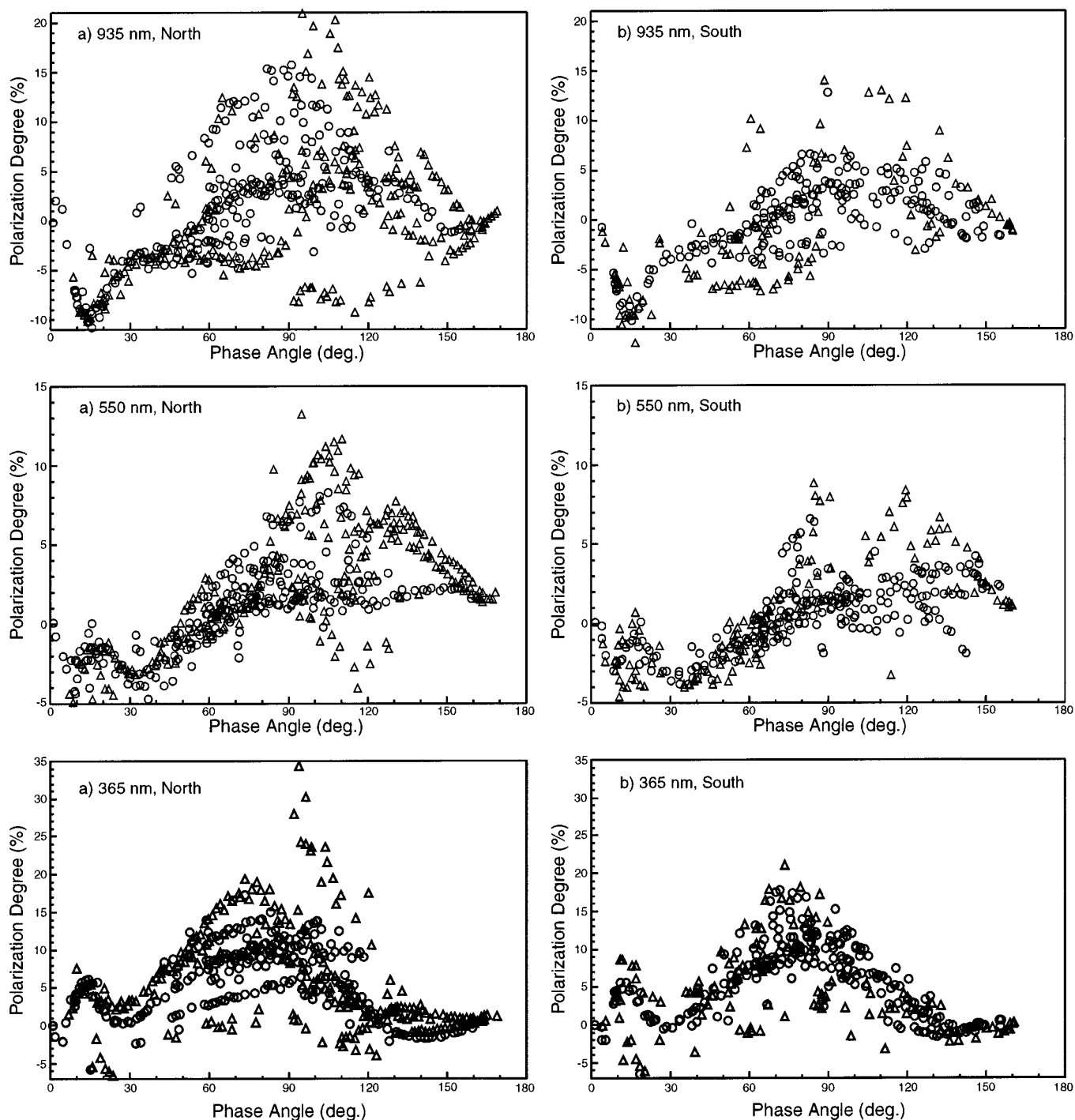
**FIG. 1.** OCPP polarimetric data at three wavelengths around polar regions. Panels (a) are around the north polar region (90°N–70°N) and panels (b) are around the south polar region (70°S–90°S). Circles indicate data at a morning terminator and triangles indicate data at an evening terminator phase.

scatterings lose their polarization features and become essentially unpolarized, the features of the linear polarization are mostly determined by the first several orders of scattering, and at most by layers down to optical thickness of order unity. Thus, it is not necessary for us to use a detailed

model for the base cloud that includes all of the structure inferred from the *in situ* measurements by various probes and landers. Furthermore, at the pressure level of the cloud tops on Venus (cf. Hansen and Hovenier 1974, Paper 1), the contribution from Rayleigh scattering by molecules to
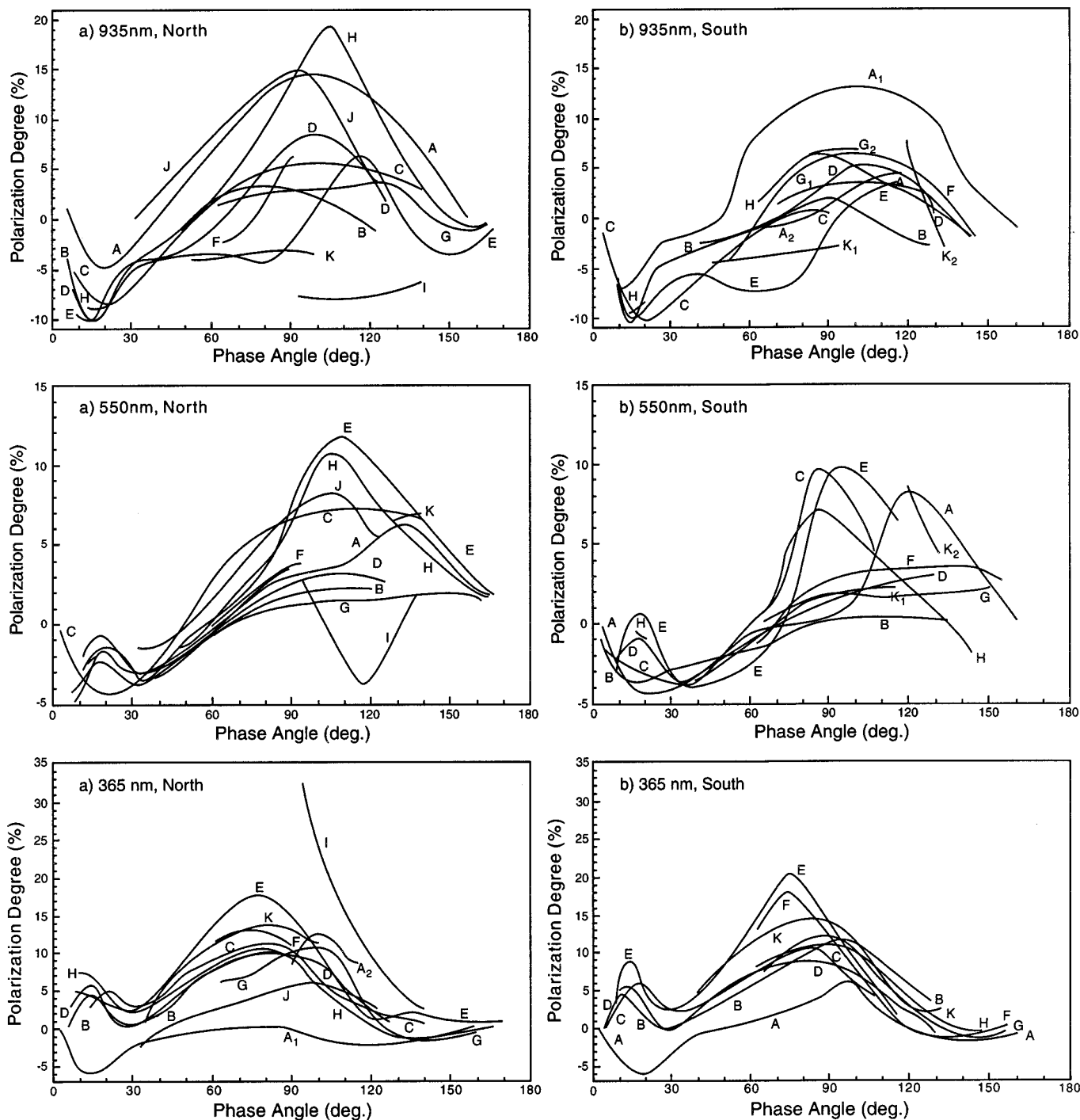
FIG. 2. Temporal grouping of OCPP polarimetric data according to observation periods. Details of each branch are listed in Table II. Panels (a) are around the north polar region (90°N–70°N) and panels (b) are around the south polar region (70°S–90°S).

the observed polarization is quite small at 935 nm, but since Rayleigh scattering is proportional to $\lambda^{-4}$, it is not negligible at 550 nm and at 365 nm. Thus, our strategy is to use the data at 935 nm to determine the properties of the haze particles and then to deduce vertical structure

information from the Rayleigh scattering contributions at 550 and 365 nm, as well as to verify the consistency of the haze characteristics derived from the 935 nm modeling.

It is neither computationally practical nor likely warranted by actual physical conditions to attempt to derive

TABLE II
Average Optical Thicknesses for Branches at 935 nm

| Branch | Orbit-number | Number of Maps (North) | Average τ (North) | Number of Maps (South) | Average τ (South) |
|--------|--------------|------------------------|-------------------|------------------------|-------------------|
| A | 0001 - 0620 | 06 / 40 / 66 | 0.37 / 0.26 | 06 / 25 / 34 | 0.29 / 0.22 |
| B | 0621 - 0745 | 16 / 29 / 47 | 0.13 / 0.16 | 16 / 24 / 37 | 0.08 / 0.08 |
| C | 0746 - 0830 | 06 / 42 / 50 | 0.12 / 0.10 | 06 / 11 / 21 | 0.07 / 0.09 |
| D | 0831 - 0969 | 17 / 27 / 46 | 0.09 / 0.10 | 17 / 49 / 65 | 0.10 / 0.12 |
| E | 0970 - 1075 | 17 / 56 / 98 | 0.04 / 0.06 | 17 / 16 / 35 | 0.03 / 0.03 |
| F | 1076 - 1160 | 08 / 15 / 15 | 0.07 / 0.08 | 08 / 29 / 34 | 0.07 / 0.13 |
| G | 1161 - 1380 | 00 / 34 / 45 | **** / 0.10 | 00 / 20 / 24 | **** / 0.12 |
| H | 1381 - 1649 | 08 / 22 / 36 | 0.10 / 0.18 | 08 / 33 / 35 | 0.22 / 0.14 |
| I | 1650 - 1780 | 00 / 00 / 19 | **** / **** | 00 / 00 / 00 | **** / **** |
| J | 1781 - 1850 | 00 / 35 / 35 | **** / 0.31 | 00 / 00 / 00 | **** / **** |
| K | 1851 - 2820 | 05 / 27 / 32 | 0.03 / 0.04 | 05 / 27 / 29 | 0.03 / 0.05 |

a unique model of the physical properties and vertical structure of the haze for each polarimetry map. Rather, our primary objective is to characterize the long-term behavior using the simple three-layer model to fit all of the data in each polar region independently under the assumption that the temporal variation of observed polarization at 935 nm is mainly due to the variation of optical thickness of the haze layer. That is, the physical properties of the haze particles, namely, the effective radius $r_{eff}$, the effective variance of haze particle size distribution $v_{eff}$, and the real part of the refractive index $n_r$, are assumed to be constant for the entire observation period. While it is reasonable to expect that the refractive index of the haze particles is essentially constant over very long time periods, we might well find that temporal variation of particle size is not only plausible, but perhaps likely. But if such variation in haze particle size is modest, then we may expect that our simple model can describe fairly well most of the features of the angular distribution of polarization degree at 935, 550, and 365 nm and provide long-term average particle properties that will serve as a starting point in returning to examine smaller groups of maps for short-term variations.

The 1-$\mu$m cloud particles on Venus have been unambiguously identified as spherical based on the distinctive cloudbow feature in the angular distribution of their polarization (Hansen and Hovenier 1974, Paper 1). The polarization signature of the haze particles is consistent with the assumption that they are spherical, although for these smaller particles, modest non-sphericity would be harder to detect (Mishchenko and Travis 1994). We assume both haze and cloud particles are in fact spherical and thus use Mie theory to compute the single-scattering properties.

Base-cloud particles have an effective radius of 1.05 $\mu$m; the effective variance of the size distribution (taken to be represented by the standard gamma function) is 0.07; the real part of the refractive index is 1.43, 1.44, and 1.46 at 935, 550, and 365 nm, respectively. These properties were

deduced by Hansen and Hovenier (1974) from a detailed analysis of ground-based polarimetry. The existence and narrow size distribution of these particles was confirmed by the *in situ* Pioneer Venus probe measurements reported by Knollenberg *et al*. (1980). Particle single scattering albedo, which is necessary in performing the multiple scattering computation, is derived by forcing the values of the computed spherical albedo to match the observed spherical albedo: 0.90, 0.87, and 0.57 at 935, 550, and 365 nm, respectively (cf. Travis 1975, Moroz 1983). We begin with the polarimetry data at 935 nm, where contribution by Rayleigh scattering is insignificant, and using the doubling-adding method (cf. Hansen and Travis 1974), we calculate the theoretical polarization corresponding to the scattering geometry of each map element for an assumed set of haze particle properties, $r_{eff}$, $v_{eff}$, and $n_r$, for 11 values of haze optical thickness $\tau_h$ in the range from 0.0 to 1.0. To measure how close the results of the theoretical computation are to the data, a weighted RMS error is introduced as

$$\varepsilon^i(\lambda, \tau_j) = \sqrt{\frac{\sum_{k=1}^{N_i} [P_{th}^{ik}(\lambda, \tau_j) - P_{ob}^{ik}(\lambda, \tau_j)]^2 [I_{ob}^{ik}(\lambda)]^2}{\sum_{k=1}^{N_i} [I_{ob}^{ik}(\lambda)]^2}}, \quad (1)$$

where $i$, $j$, and $k$ indicate the $i$th map, the $k$th pixel, and the $j$th optical thickness, respectively. $N_i$ is the total number of pixels for the $i$th map, and $P_{th}^{ik}(\lambda, \tau_j)$, $P_{ob}^{ik}(\lambda, \tau_j)$, and $I_{ob}^{ik}(\lambda)$ are theoretical polarization, observed polarization, and observed intensity for the $k$th pixel of the $i$th map for given optical thickness $\tau_j$, respectively. We employ weighting by intensity because pixels with low intensity will typically have somewhat less accurate observed polarization.

The average theoretical and observed polarizations for a map are defined by

$$P_{th}^i(\lambda, \tau_j) = \frac{\sum_{k=1}^{N_i} P_{th}^{ik}(\lambda, \tau_j) I_{th}^{ik}(\lambda, \tau_j)}{\sum_{k=1}^{N_i} I_{th}^{ik}(\lambda, \gamma_j)} \quad (2)$$

$$P_{ob}^i(\lambda) = \frac{\sum_{k=1}^{N_i} P_{ob}^{ik}(\lambda) I_{ob}^{ik}(\lambda)}{\sum_{k=1}^{N_i} I_{ob}^{ik}(\lambda)}, \quad (3)$$

where $I_{th}^{ik}(\lambda, \tau_j)$ is theoretical intensity for the $k$th element of the $i$th map for a given $\tau_j$, and $I_{ob}^{ik}(\lambda)$ is observed intensity for the $k$th element of the $i$th map at the wavelength $\lambda$. Minimum RMS error $\varepsilon_{min}^i(\lambda)$ for the $i$th map is obtained by quadratic interpolation over the set of $\varepsilon^i(\lambda, \tau_j)$ associated with the 11 optical thicknesses for the $i$th map and the optical thickness corresponding to that minimum is thus the $\tau_h$ that provides the best fit for the specified $r_{eff}$, $v_{eff}$, and $n_r$ values for that map. Haze optical thickness is thus treated as a map-dependent parameter with the expectation that the most significant temporal variation is adequately simulated. We also find the theoretical polarization $P_{th}^i(\lambda)$ corresponding to $\varepsilon_{min}^i(\lambda)$ for the map by a similar quadratic interpolation in the set of $P_{th}^i(\lambda, \tau_j)$.

Now we must define an appropriate quantitative measure of how well a model with a given set of $r_{eff}$, $v_{eff}$, and $n_r$ fits the entire set of maps for each of the polar regions. One obvious possibility is the average of $\varepsilon_{min}^i(\lambda)$ over all maps, or we might instead use a new RMS error based upon the zone-averaged observed and theoretical polarization for each map, with the square differences summed over all maps,

$$\varepsilon_0(\lambda) = \sqrt{\frac{\sum_{i=1}^{M} [P_{th}^i(\lambda) - P_{ob}^i(\lambda)]^2}{M}}, \quad (4)$$

where $M$ is the total number of maps. After experimenting with both of these measures of fit, we adopted the latter because the minimum $\varepsilon_0(\lambda)$ value seems to give a better fit of the theoretical polarizations for most of the data over the entire phase diagram.

Once we have found the set of haze particles properties, $r_{eff}$, $v_{eff}$, and $n_r$, that best fit the maps for 935 nm, we turn to consider the data at 550 and 365 nm. Effective radius and variance of the size distribution retrieved from the fit at 935 nm must of course be the same at the two shorter wavelengths. Although refractive index is wavelength dependent, we expect that the values at 550 and 365 nm will not prove to be markedly different from that found for 935 nm. Haze optical thickness for a single map is not a

free parameter, but should be scaled by the ratio of the extinction cross sections following

$$\tau(\lambda) = \frac{Q_{ext}(\lambda)}{Q_{ext}(\lambda_0)} \tau(\lambda_0), \quad (5)$$

where $Q_{ext}(\lambda_0)$ and $Q_{ext}(\lambda)$ are the cross sections for single scattering at wavelengths $\lambda_0$ and $\lambda$, respectively. Absent other considerations, the normal strategy for analyzing the data at 550 and 365 nm would be to first scale the optical thickness of an individual map at 935 nm to those appropriate for 550 and 365 nm, and then a gas layer of optical thickness $\tau_R$ for Rayleigh scattering is placed above the scaled haze layer and allowance for the contribution to the polarization due to Rayleigh scattering by gas within the haze layer is parameterized by the Rayleigh fraction $f_{Rh}$ for each map to obtain the best fitting gas amount. With this approach, each map has its own haze optical thickness, overlying gas layer, and Rayleigh fraction, so that there would be 327 different models for the north polar region for each wavelength. Because of the excessive computational demands that this would impose, we have instead adopted an approach in which we create several groups, each composed of maps with relatively similar $\tau_h$ values at 935 nm. Then for each group, we derive the best fitting model in a manner analogous to that used in the 935 nm analysis. That is, the temporal variation of polarization for maps at 550 and 365 nm is assumed to be mostly due to the variation of the gas layer optical thickness, which is retrieved for each map through minimization of the observed vs theoretical polarization differences. The optical thickness of the haze layer is fixed at the scaled value using Eq. (5) for the average $\tau_h$ at 935 nm for all of the maps in the group.

## 4. ANALYSIS

Finding the minimum value of $\varepsilon_0$ in the three dimensional parameter space $(r_{eff}, v_{eff}, n_r)$ is of course a computationally intensive problem. Since $\varepsilon_0$ is far from being a simple analytic function, we cannot expect to determine a precise convergence point, but rather look for the approximate region which has the minimum error between observed and theoretical polarization for all of the maps. The search covers the following ranges of physical parameters: $0.0 < r_{eff} \le 1.0$ ($\mu$m), $0.0 < v_{eff} \le 0.5$, and $1.1 < n_r \le 2.0$, which are chosen to be sufficiently broad to ensure that the best fitting values are encompassed. This parameter space is divided into $5 \times 5 \times 5$ smaller cubes and for $6 \times 6 \times 6$ grid points within each cube. The Powell method (cf. Beveridge and Schechter 1970) is applied to optimize the search for the point which gives the minimum value

of $\varepsilon_0$. The Powell method provides optimum convergence with computations required at a minimum number of grid points if the optimization function is approximately quadratic in behavior. However, in view of the likely complex functional behavior of $\varepsilon_0$ we make additional direct computations at many other grid points to ensure that the solution is reasonably well behaved.

We find that the best-fitting model for the 327 maps for the north polar region has physical parameters for the haze of $r_{eff} = 0.25 \pm 0.05$ $\mu$m, $v_{eff} = 0.25 \pm 0.10$, and $n_r = 1.43 \pm 0.01$ at 935 nm, and the logarithmic average of haze optical thickness over all maps is $\langle \tau_h^{935} \rangle = 0.101 \pm 0.02$. The uncertainty estimates indicated for each parameter are based upon the variation in the value of the respective parameter for $\varepsilon_0$ values within 15% of the minimum error. If the parameters of this best fitting model are used for the larger set of maps that includes those with phase angles $\leq 30°$, the value of $\varepsilon_0$ is increased by only 3% from that for the set of 327. Thus, despite the fact that the haze polarization signature is less distinctive at small phase angles, the retrieved haze particle properties are nonetheless consistent with the observed polarization for those maps.

A similar analysis of the 234 maps for the south polar region yields physical values $r_{eff} = 0.29 \pm 0.02$ $\mu$m, $v_{eff} = 0.25 \pm 0.03$, and $n_r = 1.43 \pm 0.01$ at 935 nm and $\langle \tau_h^{935} \rangle = 0.0964 \pm 0.015$. Haze particle effective radius found for the south polar region is slightly larger than that for the north, although within the estimated uncertainties, they are similar and in approximate agreement with the result we found in Paper 1, viz., $0.23 \pm 0.04$ $\mu$m. Best fitting size distribution variance and refractive indices are identical for two polar regions and the long-term average haze optical thicknesses are similar. Haze particle size is consistent with the analysis of OCPP limb scan data by Lane and Opstbaum (1983). Krasnopolsky (1983) inferred a size of 0.25 $\mu$m for the upper haze particles by analyzing spectroscopy data obtained by Veneras 9 and 10.

Henceforth, we focus on the data for the north polar region in order to verify the consistency of the haze particle properties deduced from the data at 935 nm and derive vertical structure information from the contribution to the observed polarization by Rayleigh scattering at the two shorter wavelengths. Each model now explicitly includes a layer of gas above the haze as well as the contribution from gas within the haze layer as represented by the Rayleigh fraction. Additional parameters to be derived are the haze particle refractive indices at 550 and 365 nm. The only computationally practical strategy is to use a haze layer with a fixed, average optical thickness for a set of maps and assume that all of the temporal variability in the observed polarization at 550 and 365 nm can be explained by map-dependent optical thickness of the gas layer. Although we will ultimately find that it is necessary to use

sets of maps sorted on the basis of similar haze optical thicknesses found from 935 nm analysis, we begin by considering a set that includes all of the maps and uses the corresponding long-term average haze optical thickness.

Using essentially the same approach employed to find haze layer optical thickness at 935 nm, we determine a best fitting $\tau_R$, Rayleigh scattering optical thickness of the gas layer, from a set of models computed for 11 values of $\tau_R$ by interpolating to find the minimum RMS error for each map. Then we find the haze particle refractive index and Rayleigh fraction $f_{Rh}$ which correspond to the minimum $\varepsilon_0(\lambda)$ the entire set of maps. Operationally, it is most straightforward to perform this procedure for 550 and 365 nm independently. However, since the Rayleigh scattering coefficient scales as $\lambda^{-4}$, the optical thicknesses of the gas layer at the two wavelengths are obviously not independent. Initial best fitting models do not satisfy the requisite wavelength-dependent scaling for the Rayleigh scattering components, so we iterate the procedure with parameter adjustments within 25% of the value corresponding to the initial minimum $\varepsilon_0$ in order to obtain the best compromise within uncertainty estimates. For the set of 327 maps for the north polar region, the model parameters that yield the best fit are: $n_r^{550} = 1.435 \pm 0.02$, $\langle \tau_R^{550} \rangle = 0.00193$ at 550 nm and $n_r^{365} = 1.450 \pm 0.025$, $\langle \tau_R^{365} \rangle = 0.0102$, and $f_{Rh}^{365} = 0.043$ at 365 nm. Haze optical thicknesses, $\langle \tau_h^{550} \rangle = 0.234$ and $\langle \tau_h^{365} \rangle = 0.294$, have been scaled from the average of 0.102 for all maps at 935 nm. Rayleigh fraction at 550 nm for the haze layer is too small to be reliably determined directly, but from scaling using the value found for 365 nm it would be ~0.008.

Figure 3a shows the theoretical polarization degree values for our best fitting unified model for the north polar region and observational data plotted in P–P diagrams at all three wavelengths. Circles, triangles, and X's are observations on the morning side of the terminator, the evening terminator, and their corresponding theoretical values, respectively. Figure 3b displays the absolute difference $P_{th}^i - P_{ob}^i$ against phase angle. We note that only 6, 1, and 11 maps out of 327 maps have more than 2% absolute difference at 935, 550, and 365 nm, respectively. This indicates that the present model provides a relatively good fit to the data at all wavelengths despite its limitations with respect to the single, average haze layer for 550 and 365 nm.

Location of the haze layer in terms of atmospheric pressure can be derived from the relation between gas optical thickness for Rayleigh scattering and pressure (cf. Hansen and Travis 1974)

$$P(mb) = \frac{6.17 \times 10^4 \, \lambda^4}{1 + 0.013 \, \lambda^{-2}} \, \tau_R, \qquad (6)$$

where $\lambda$ is in micrometers. So the $\langle \tau_R^{365} \rangle$ value of 0.0101
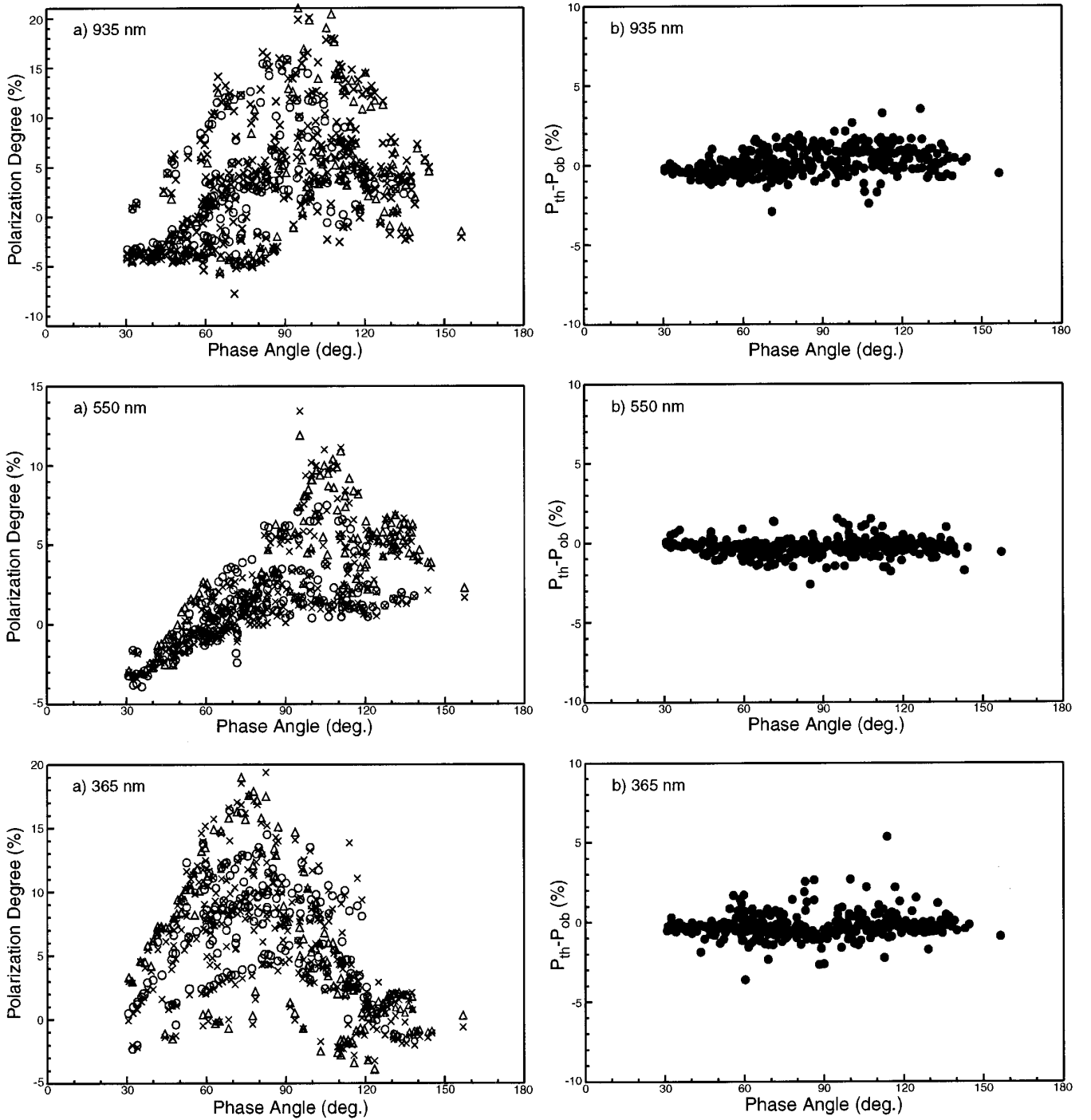
**FIG. 3.** All OCPP polarimetric data (open circles and triangles) used for the present analysis compared with theoretical polarization (X's). A total of 327 maps have complete data at all three wavelengths around the northern polar region. (a) Absolute values of observation and theoretical polarization. (b) The differences between theoretical polarization and observation data are plotted with phase angle.

indicates that the top of the haze layer for the present model is at ~10 *mb*. Within the haze layer, the Rayleigh fraction $f_{Rh}$ is simply converted into an equivalent optical thickness $\tau_{Rh}^{365}$ from the relation:

$$\tau_{Rh}^{365} = \frac{f_{Rh}}{1 - f_{Rh}} \tau_{h}^{365}. \qquad (7)$$

So the Rayleigh optical thickness of the gas within the

haze layer is $\langle \tau_{Rh}^{365} \rangle \sim 0.013$, corresponding to 13 *mb*, which therefore places the top of the cloud layer at the 23 *mb* level.

Although the agreement represented by Fig. 3 is by no means poor, the compromises associated with using scaled haze layer optical thickness at 550 and 365 nm based upon a single average at 935 nm over all 327 maps are apparent. Therefore, we attempt to improve the approach without incurring prohibitive computational demands by dividing the maps into several groups according to the optical thickness of the haze particles at 935 nm. Specifically, let us investigate the following three cases in more detail: **(1)** Thick haze model, denoted $T_k$: The group $T_k$ consists of 23 maps with optical thickness of the haze layer at 935 nm in the range 0.25–0.35. This group consists of parts of branches $A(15)$, $H(7)$, and $J(1)$. (Parenthetical entries are the numbers of maps included from that branch.) **(2)** Medium haze model, denoted $M_m$: The group $M_m$ consists of 56 maps with optical thickness of the haze layer at 935 nm in the range 0.07–0.13. This group consists of parts of branches $B(8)$, $C(15)$, $D(6)$, $E(2)$, $G(14)$, $H(8)$, and $J(3)$. **(3)** Thin haze model, denoted $T_n$: The group $T_n$ consists of 56 maps with optical thickness of the haze layer at 935 nm in the range 0.04–0.06. This group consists of parts of branches $B(3)$, $C(2)$, $D(2)$, $E(28)$, $F(6)$, $H(2)$, and $K(13)$.

Since the maps within each of the three groups have relatively similar haze optical thicknesses at 935 nm, the assumption that polarizations at 550 and 365 nm are mostly due to the temporal variation of the optical thickness of gas above the haze layer is likely to be more realistic for these groups than for the unified model. The same procedure described above was used to obtain a best fitting model for each group. Indeed, we now find that it is much easier to derive the amount of the gas above the haze, Rayleigh fraction inside the haze layer, and refractive indices of the haze particles while preserving the appropriate scaling relation between average optical thickness of the gas layer at 550 nm and that at 365 nm. The results of the analysis for these three groups will be summarized later along with those for the unified model, denoted $U_d^n$ for the north polar region and $U_d^s$ for the south. Also, theoretical and observed polarization degree values are plotted in P–P diagrams separately for the three groups in Figs. 4a, 5a, and 6a, using circles, triangles, and X's as defined for Fig. 3a. Figures 4b, 5b, and 6b show the absolute difference between theoretical polarization values and observational data plotted against phase angle. The maximum absolute values of the differences for all three subgroups are roughly 2, 1.5, and 3%, at 935, 550, and 365 nm, respectively. The number of maps with more than 1% absolute difference $P_{th} - P_{ob}$ are 8, 20, and 13 in groups $T_k$, $M_m$, and $T_n$, respectively. Just 9 of those 41 maps have more than 1.5% absolute difference and could benefit from a model with different physical properties of the haze particles: 7 out of

these 9 would have improved fits for particles with $r_{eff} = 0.26$ $\mu$m, $v_{eff} = 0.28$, and $n_r = 1.44$ at 935 nm. The other two maps need a smaller particle size, viz., $r_{eff} = 0.24$ $\mu$m, to show good agreement between the data and theoretical values. These rather modest changes are still within the estimated uncertainties of these parameters, thus suggesting that our basic assumption that temporal variation of haze particle physical properties should be relatively small is in fact justified.

Because of the relatively smaller number of maps for the south polar region, we considered only the single unified model for those observations rather than attempting to define several groups as for the north polar region. Specifically, we find the following physical quantities for the unified model for the south polar region $U_d^s$: (a) refractive indices and optical thicknesses of the haze particles were $n_r^{550} = 1.45 \pm 0.02$, $\langle \tau_h^{550} \rangle = 0.206$ at 550 nm and $n_r^{365} = 1.455 \pm 0.02$, $\langle \tau_h^{365} \rangle = 0.232$ at 365 nm. (b) Rayleigh optical thickness of the gas layer was $\langle \tau_R^{550} \rangle = 0.00143$ and $\langle \tau_R^{365} \rangle = 0.00705$. (c) Rayleigh fraction of the haze layer was $f_{Rh}^{365} = 0.118$. Using Eq. (7) and the above values, we find the optical thickness of gas within the haze layer in the south polar region is $\tau_{Rh}^{365} = 0.031$.

All results of the physical properties and vertical structure of the haze layer are summarized in Table III. We note that in addition to having slightly larger haze particles in the south polar region, the top of the haze layer there is slightly higher, while the top of the cloud layer is somewhat lower. Also, the refractive indices at 550 and 365 nm for the south polar haze are slightly larger than those for the unified north polar region model, but by amounts that are within estimated uncertainties as well as being on the same order as the variation among the thick, medium, and thin north polar region models.

## 5. CONCLUSIONS

Based upon the assumption that the variation of the observed polarization at 935 nm is mainly due to temporal variation of optical thickness of the haze layer, we have analyzed the OCPP polarimetry observations of the polar regions of Venus. Our objective has been to construct the simplest model which can explain polarization observations at three wavelengths over a broad range of phase angles for a period covering the first 2820 orbits (nearly eight years) of the Pioneer Venus mission. In this context, we have adopted particle characteristics for the base cloud deduced from earlier analysis of ground-based polarimetry (Hansen and Hovenier, 1974) and confirmed by *in situ* measurements (Knollenberg and Hunten, 1980) and thus focus on a detailed retrieval of the polar haze characteristics. As described in the previous section and summarized in Table III, the haze particle properties are consistent with the prior identification of concentrated sulfuric acid
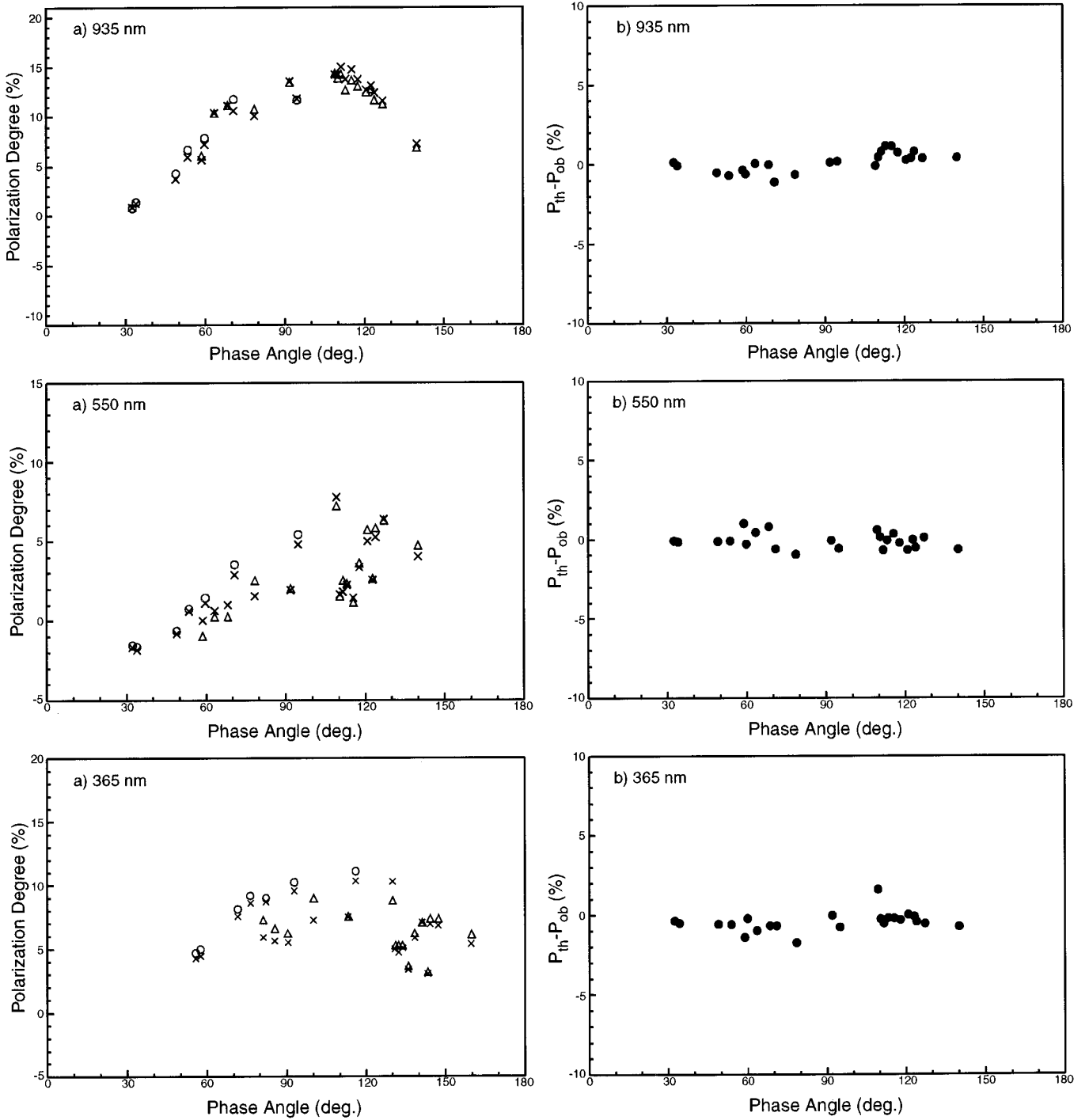
**FIG. 4.** OCPP polarimetric data (open circles and triangles) with the optical thickness of the haze layers $0.25 \leq \tau_h^{935} \leq 0.35$ in comparison with the theoretical polarization (X's). A total of 23 maps fall in this range of optical thickness. (a) Absolute values of observation and theoretical polarization. (b) The differences between theoretical polarization and observation data are plotted with phase angle.
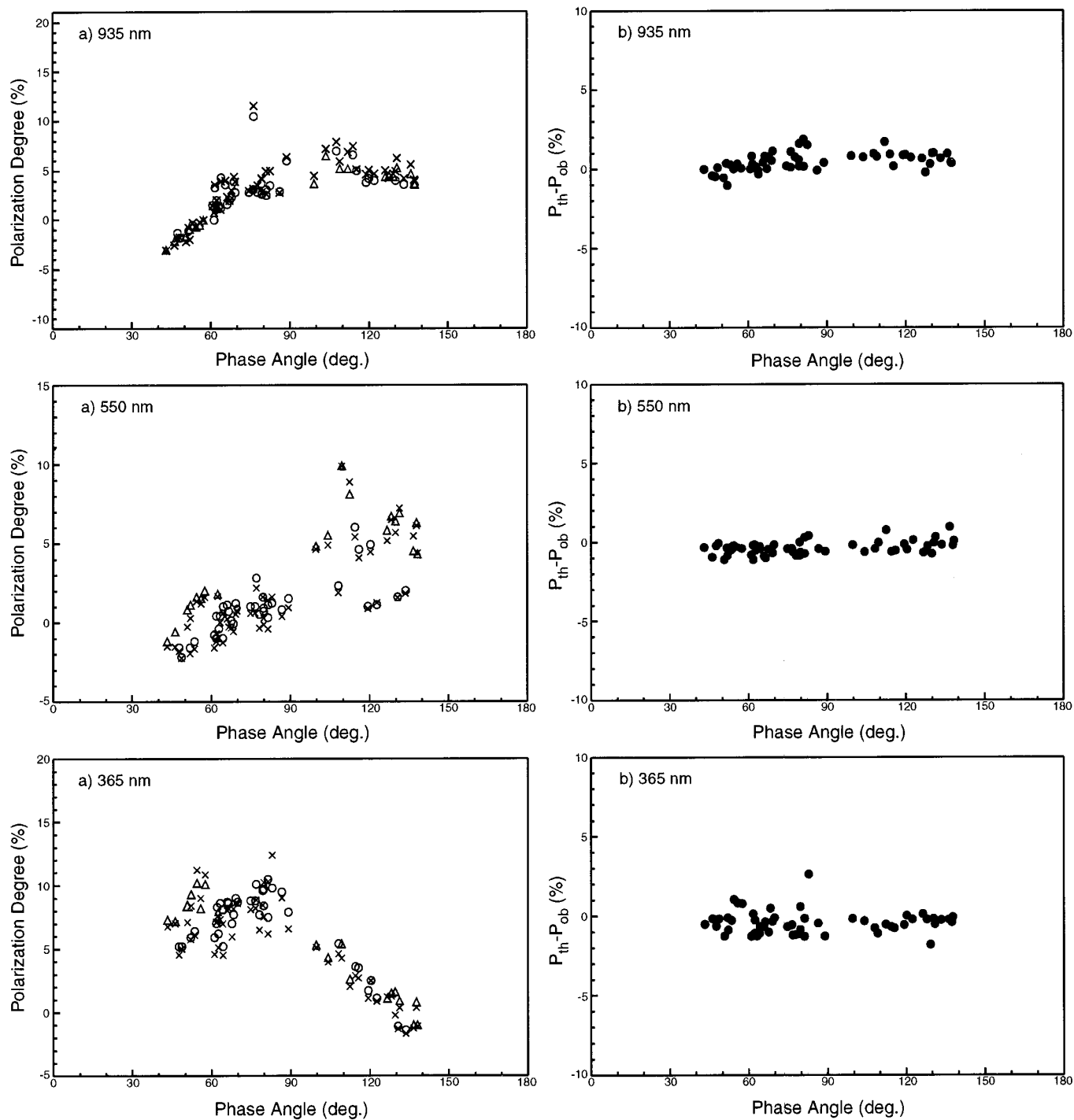
**FIG. 5.** OCPP polarimetric data (open circles and triangles) with the optical thickness of the haze layers $0.07 \le \tau_h^{935} \le 0.13$ in comparison with the theoretical polarization (X's). A total of 56 maps fall in this range of optical thickness. (a) Absolute values of observation and theoretical polarization. (b) The differences between theoretical polarization and observation data are plotted with phase angle.
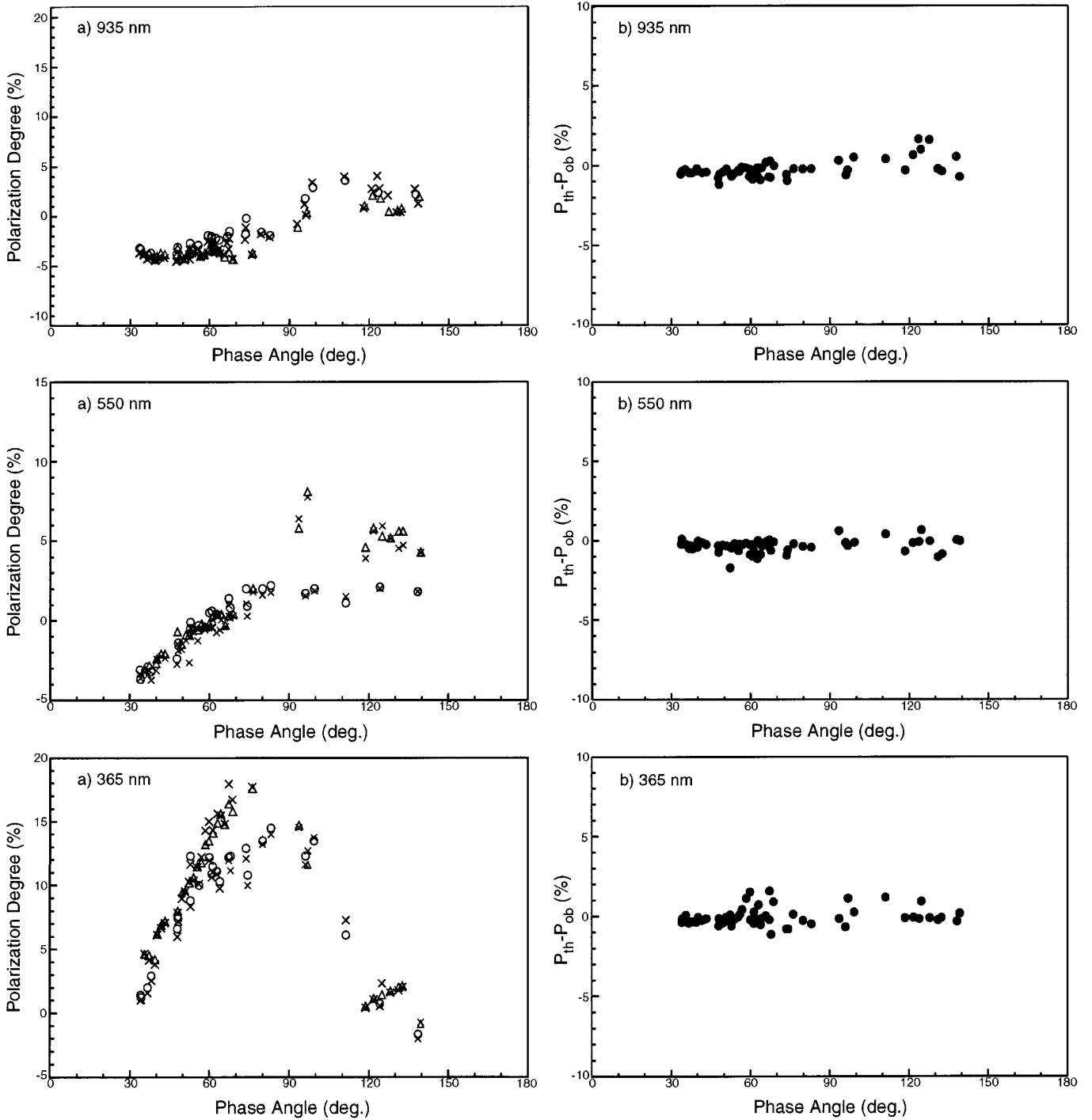
**FIG. 6.** OCPP polarimetric data (open cirlces and triangles) with the optical thickness of the haze layers $0.04 \leq \tau_h^{935} \leq 0.06$ in comparison with the theoretical polarization (X's). A total of 56 maps fall in this range of optical thickness. (a) Absolute values of observation and theoretical polarization. (b) The differences between theoretical polarization and observation data are plotted with phase angle.

and do not appear to exhibit significant change over time, with the major temporal variation being attributable to variation in the thickness of the haze layer. There are only minor differences between the physical properties of the

haze particles for the two polar regions. The retrieved haze particle properties and model vertical structure were applied to data for the north polar region for 26 other maps selected from orbit numbers 3350–4200. Only six

TABLE III

Summary of the Physical Quantities and Vertical Structures of the Haze Particles around Both Polar Regions

| Physical Parameters of the Haze Particles | | North Pole | | | | South Pole |
|---|---|---|---|---|---|---|
| | | $U_d^n$ (All) | $T_k$ (Thick) | $M_m$ (Medium) | $T_n$ (Thin) | $U_d^r$ (All) |
| Branches used for Model | | All except I | A, J, H | B, C, D, E, G, H, J | B, C, D, E, F, H, J | All except I & J |
| Number of Maps | N | 327 | 23 | 56 | 56 | 234 |
| Effective Radius ($\mu$m) | $r_{eff}$ | 0.25±0.05 | 0.25±0.05 | 0.25±0.05 | 0.25±0.05 | 0.29±0.02 |
| Effective Variance | $v_{eff}$ | 0.25±0.10 | 0.25±0.10 | 0.25±0.10 | 0.25±0.10 | 0.25±0.03 |
| Refractive Index | $n_r^{935}$ | 1.430±0.010 | 1.430±0.010 | 1.430±0.010 | 1.430±0.010 | 1.430±0.010 |
| | $n_r^{550}$ | 1.435±0.020 | 1.450±0.010 | 1.445±0.010 | 1.435±0.010 | 1.450±0.020 |
| | $n_r^{365}$ | 1.450±0.025 | 1.465±0.015 | 1.450±0.020 | 1.470±0.010 | 1.455±0.020 |
| Optical Thickness of the Haze Layer | $\tau_h^{935}$ | 0.10±0.02 | 0.30±0.01 | 0.10±0.01 | 0.05±0.01 | 0.10±0.02 |
| | $\tau_h^{365}$ | 0.29±0.05 | 0.90±0.03 | 0.30±0.03 | 0.16±0.03 | 0.23±0.04 |
| Rayleigh Fraction | $f_{Rh}^{365}$ | 0.04±0.02 | 0.01±0.01 | 0.04±0.02 | 0.10±0.04 | 0.12±0.04 |
| Optical Thickness of the Gas Layer | $<\tau_R^{550}>$ | 0.002 | 0.002 | 0.002 | 0.004 | 0.001 |
| | $<\tau_R^{365}>$ | 0.010 | 0.008 | 0.011 | 0.019 | 0.007 |
| | $<\tau_{Rh}^{365}>$ | 0.013 | 0.011 | 0.013 | 0.018 | 0.031 |
| Pressure Level of the Top of a Layer | Haze | ~10 mb | ~8 mb | ~11 mb | ~19 mb | ~7 mb |
| | Cloud | ~23 mb | ~19 mb | ~24 mb | ~37 mb | ~38 mb |

maps out of the 26 have more than 2% absolute difference between the observed and theoretical polarizations and the total RMS error increased by only 7%, implying that the present model derived from analysis of the data from orbit numbers 1–2820 can probably still describe the data from later years.

Temporal variation of the haze layer optical thickness may appear to have a decreasing trend over the long term in both polar regions (Fig. 7a, and 7b), but the statistics to support such a conclusion are meager. Optical thickness vs phase angle (Fig. 7c) reveals no systematic pattern that could raise concern about retrieval sensitivity to observation geometry. While there may be a qualitative indication of optical thickness increasing or decreasing with quasi-oscillations of roughly 170 to 200 days, lack of continuous coverage makes such a characterization very tentative at best. Only maps in the periods with orbit numbers around 700–900 in the north and 1100–1200 in the south show clear peaks of the oscillations of haze optical thickness. It has been suggested that there might be a correlation of excessive haze with exceptional polar brightness (Dollfus et al. 1979, Paper 1), but we have been unable to establish such a correlation for the OCPP maps studied here.

If we plot optical thickness for maps in the north polar region vs that for the south (i.e., for the 83 maps with same orbit numbers) as shown in Fig. 8, there certainly seems to be a correlation. Indeed, we find that the correlation index is 0.7. Such a correlation raises interesting questions about a possible mechanism that can affect vertical structure and/or haze production contemporaneously at both polar regions. If the apparent quasi-oscillation period is truly on the order of $10^6$–$10^7$ sec, then this would be similar to the time scale of the meridional circulation of the Venus atmosphere (Schubert et al. 1980, Del Genio and Rossow 1990), suggesting a dynamical modulation that could be symmetric. Esposito (1984) has suggested a link between $SO_2$ from possibly current volcanism on Venus and variation in $SO_2$ abundance in the cloud-top region. Although Magellan radar images may provide evidence of geologically recent volcanic eruptions and outflows (Smrekar 1994, Robinson et al. 1993, 1995), we have no direct evidence that such active volcanism presently is occurring. Further, there is some question regarding the magnitude of eruption that would be necessary to carry $SO_2$ to the cloud-top altitude through the stable atmospheric layer below the cloud levels (Robinson et al. 1995). Perhaps another possibility is variation in solar ultraviolet radiation that plays a role in creating the free oxygen necessary to convert $SO_2$ to sulfuric acid in the haze layer region.

Through the present analysis of the OCPP polarimetry observations from the Pioneer Venus mission, we have been able to establish that the submicrometer haze in the polar regions has relatively stable physical characteristics despite its rather substantial temporal variation in the amount visible above the base cloud of larger sulfuric acid particles. Nonetheless, there are indications that further investigation of short-term variations and the more complex models that may be necessary to explain them as well as examination of lower latitude regions are required to

## Temporal Variation of Haze Optical Thickness



FIG. 8. Correlation between optical thicknesses of maps with same orbit numbers in north and south polar regions (log scale is used in both axes).
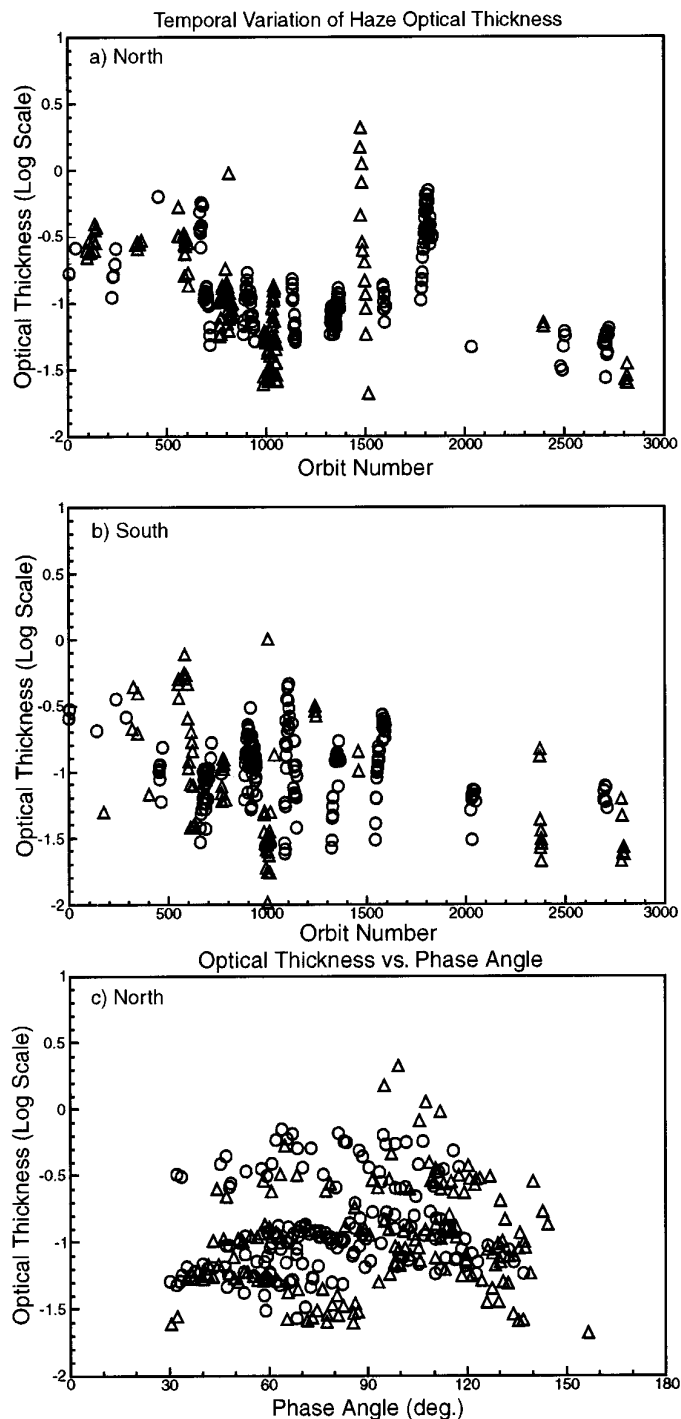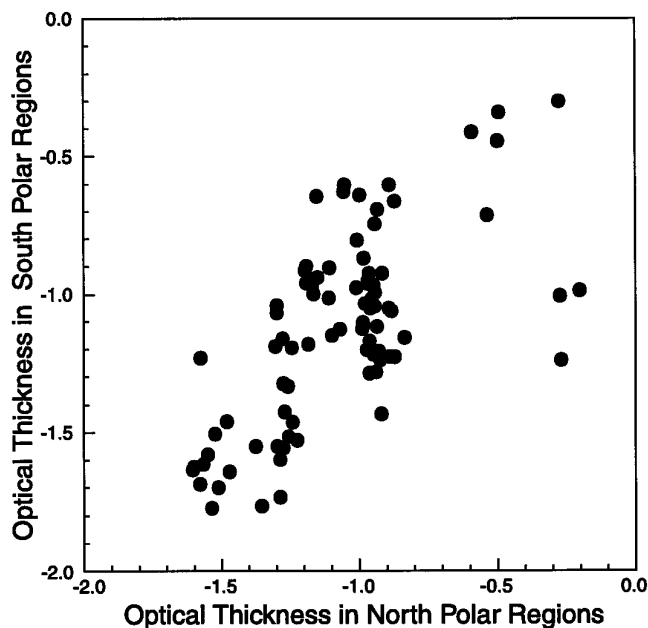
FIG. 7. Haze optical thickness of the data is plotted against the orbit number: (a) In the northern polar region (327 maps) and (b) in the southern polar region (234 maps). (c) Optical thickness in the northern polar region is plotted against phase angle. Circles indicate data at a morning terminator and triangles indicate data at an evening terminator phase.

complete the picture regarding the haze and cloud tops on Venus.

## ACKNOWLEDGMENTS

## REFERENCES

ANDREICHIKOV, B. M., I. K. AKHMETSHIN, B. N. KORCHUNGANOV, L. M. MUKHIN, B. I. OGORODNIKOV, I. V. PETRYANOV, AND V. I. SKITOVICH 1987. X-ray radiometric analysis of Venus cloud aerosol by Vega-1 and -2 automated interplanetary probes. *Kosm. Issled.* **25**, 721–736.

BEVERIDGE, G. S. G., AND R. S. SCHECHTER 1970. *Optimization: Theory and Practice.* McGraw-Hill, New York.

BÉZARD, B., C. DE BERGH, D. CRISP, AND J. P. MAILLARD 1990. The deep atmosphere of Venus revealed by high-resolution nightside spectra. *Nature* **345**, 508–511.

CARLSON, R. W., K. H. BAINES, TH. ENCRENAZ, F. W. TAYLOR, P. DROSSART, L. W. KAMP, J. B. POLLACK, E. LELLOUCH, A. D. COLLARD, S. B. CALCUTT, D. H. GRINSPOON, P. R. WEISSMAN, W. D. SMYTHE, A. C. OCAMPO, G. E. DANIELSON, F. P. FANALE, T. V. JOHNSON, H. H. KIEFFER, D. L. MATSON, T. B. MCCORD, AND L. A. SODERBLOM 1991. Galileo infrared imaging spectrometer measurements at Venus. *Science* **253**, 1541–1548.

CARLSON, R. W., L. W. KAMP, K. H. BAINES, J. B. POLLACK, D. H. GRINSPOON, TH. ENCRENAZ, P. DROSSART, AND F. W. TAYLOR 1993. Variation in Venus cloud particle properties: a new view of Venus's cloud morphology as observed by the Galileo Near-infrared Mapping Spectrometer. *Planet. Space Sci.* **41,** 477–485.

COFFEEN, D. L., AND T. GEHRELS 1969. Wavelength dependent of polarization. XV. Observations of Venus. *Astron. J.* **74,** 433–445.

COLIN, L. 1979. Encounter with Venus. *Science* **203,** 743–745.

DEL GENIO, A. D., AND W. B. ROSSOW 1990. Planetary-scale waves and the cyclic nature of cloud top dynamics on Venus. *J. Atmos. Sci.* **47,** 293–318.

DOLLFUS, A., AND E. MAURICE 1965. Étude de l'allangement des crones du croissant de Vénus en juin 1964. *C. R. Acad. Sci.* **260,** 427–430.

DOLLFUS, A. 1966. Contribution au Colloque Caltech-JPL sur la Lune et les Planètes: Vénus. In *Proceedings of the Caltech-JPL Lunar and Planetary Conference JPL TM 33–266*, pp. 187–202.

DOLLFUS, A., AND D. L. COFFEEN 1970. Polarization of Venus. I. Disk observations. *Astron. Astrophys.* **8,** 251–266.

DOLLFUS, A., M. AURIÉRE, AND R. SANTER 1979. Wavelength dependence of polarization. XXXVII. Regional observation of Venus. *Astron. J.* **84,** 1419–1436.

ESPOSITO, L. W., R. G. KNOLLENBERG, M. YA. MAROV, O. B. TOON, AND R. P. TURCO 1983. The clouds and hazes of Venus, In *Venus* (D. M. Hunten, L. Colin, T. M. Donahue, and V. I. Moroz, Eds.), pp. 484–564. University of Arizona Press, Tucson.

ESPOSITO, L. W. 1984. Sulfur dioxide: Episodic injection shows evidence for active Venus volcanism, *Science* **223,** 1072–1074.

GEHRELS, T., J. C. GRADIE, M. L. HOWES, AND F. J. VRBA 1979. Wavelength dependence of polarization. XXXIV. Observations of Venus. *Astron. J.* **84,** 671–682.

GOODY, R. 1967. The scale height of the Venus haze layer. *Planet. Space Sci.* **15,** 1817–1819.

GRINSPOON, D. H., J. B. POLLACK, B. R. SITTON, R. W. CARLSON, L. W. KAMP, K. H. BAINES, TH. ENCRENAZ, AND F. W. TAYLOR 1993. Probing Venus's cloud structure with *Galileo* NIMS. *Planet. Space Sci.* **41,** 515–542.

HANSEN, J. E. AND A. ARKING 1971. Clouds of Venus: Evidence for their nature. *Science* **171,** 669–672.

HANSEN, J. E., AND J. W. HOVENIER 1974. Interpretation of the polarization of Venus. *J. Atmos. Sci.* **31,** 1137–1160.

HANSEN, J. E., AND L. D. TRAVIS 1974. Light scattering in planetary atmospheres. *Space Science Rev.* **16,** 527–610.

HARTLEY, K. K., A. R. WOLFF, AND L. D. TRAVIS 1989. Croconic acid: An absorber in the Venus clouds? *Icarus* **77,** 382–390.

KAWABATA, K., D. L. COFFEEN, J. E. HANSEN, W. A. LANE, M. SATO, AND L. D. TRAVIS 1980. Cloud and haze properties from Pioneer Venus polarimetry. *J. Geophys. Res.* **85,** 8129–8140.

KNOLLENBERG, R. G., AND D. M. HUNTEN 1980. The microphysics of the clouds of Venus: Results of the Pioneer Venus particle size spectrometer experiment. *J. Geophys. Res.* **85,** 8039–8058.

KNOLLENBERG, R., L. TRAVIS, M. TOMASKO, P. SMITH, B. RAGENT, L. ESPOSITO, D. MCCLEESE, J. MARTONCHIK, AND R. BEER 1980. The clouds of Venus: A synthesis report. *J. Geophys. Res.* **85,** 8059–8081.

KRASNOPOLSKY, V. A. 1983. Venus spectroscopy in the 3000–8000 Å region by Veneras 9 and 10. In *Venus* (D. M. Hunten, L. Colin, T. M. Donahue, and V. I. Moroz., Eds.), pp. 459–483. University of Arizona Press, Tucson.

KRASNOPOLSKY, V. A. 1985. Chemical composition of Venus clouds. *Planet. Space Sci*, **33,** 109–117.

KRASNOPOLSKY, V. A., AND J. B. POLLACK 1994. $H_2O$–$H_2SO_4$ system in Venus' clouds and OCS, CO, and $H_2SO_4$ profiles in Venus' troposphere. *Icarus* **109,** 58–78.

LANE, W.A. 1979. Wavelength dependence of polarization. XXXV. Vertical structure of scattering layers above the visible Venus clouds. *Astron. J.* **84,** 683–691.

LANE, W. A., AND R. OPSTBAUM 1983. High altitude Venus haze from Pioneer Venus limb scans. *Icarus* **54,** 48–58.

LINK, F. 1969. *Eclipse Phenomena in Astronomy*. Springer-Verlag. New York.

MAROV, M. YA., B. V. BYVSHEV, K. N. MANUILOV, YU. P. BARAMOV, I. S. KUZNETSTOV, V. N. LEBEDEV, V. E. LYSTEV, A. V. MAKSIMOV, G. K. POPANDOPULO, V. A. RAZDOLIN, V. A. SANDIMIROV, AND A. M. FROLOV 1977. Nephelometric investigations on the stations of Venera 9 and Venera 10. *Cosmic Res.* **14,** 729.

MAROV, M. YA. 1978. Results of Venus missions. In *Ann. Rev. Astron. Astrophys.* (G. Burbridge, Ed.), Vol. 16, pp. 141–169. Annual Reviews Inc., Palo Alto.

MAROV, M. YA. 1979. The atmosphere of Venus: Venera data. *Fund. of Cosmic Phys.* **5,** 1–46.

MAROV, M. YA., V. E. LYSTEV, V. N. LEBEDEV, N. L. LUKSHEVICH, AND V. P. SHARI 1980. The structure and microphysical properties of the Venus clouds: Venus 9, 10, and 11 data. *Icarus* **44,** 608–639.

MARTONCHIK, J. V. 1974. Sulfuric acid cloud interpretation of the infrared spectrum of Venus. *Astrophys. J.* **193,** 495–501.

MARTONCHIK, J. V., AND R. BEER 1975. Analysis of spectrophotometer observations of Venus in the 3–4 micron region. *J. Atmos. Sci.* **32,** 1151–1156.

MISHCHENKO, M. I., AND L. D. TRAVIS 1994. Light scattering by polydisperse, rotationally symmetric nonspherical particles: linear polarization. *J. Quant. Sperctrosc. Radiat. Transfer* **51,** 759–778.

MOROZ, V. I. 1983. Stellar magnitude and albedo data of Venus: In *Venus* (D. M. Hunten, L. Colin, T. M. Donahue, and V. I. Moroz., Eds.), pp. 27–35. Univ. of Arizona Press, Tucson.

O'LEARY, B. 1975. Venus: Vertical structure of stratospheric hazes from Mariner 10 pictures. *J. Atmos. Sci.* **32,** 1091–1100.

RAGENT, B., AND J. BLAMONT 1980. The structure of the clouds of Venus: Results of the Pioneer Venus nephelometer experiment. *J. Geophys. Res*. **85,** 8089–8105.

ROBINSON, C. A., AND J. A. WOOD 1993. Recent volcanic activity on Venus: evidence from radiothermal emissivity measurements. *Icarus* **102,** 26–39.

ROBINSON, C. A., G. D. THORNHILL, AND E. A. PARFITT 1995. Large-scale volcanic activity at Maat Mons: Can this explain fluctuations in atmospheric chemistry observed by Pioneer Venus? *J. Geophys. Res.* **100,** 11755–11763.

SAGDEEV, R. Z., AND V. I. MOROZ 1986. Project Vega first stage: Missions to Venus. *Sov. Astron. Lett.* **12,** 1–2

SAMUELSON, R. E., R. A. HANEL, L. W. HERATH, V. G. KUNDE, AND W. G. MAGUIRE 1975. Venus cloud properties: Infrared opacity and mass mixing ratio. *Icarus* **25,** 49–63.

SCHUBERT, G., C. COVEY, A. DEL GENIO, L. S. ELSON, G. KEATING, A. SEIFF, R. E. YOUNG, J. APT, C. C. COUNSELMAN III, A. J. KLIORE, S. S. LIMAYE, H. E. REVERCOMB, L. A. SROMOVSKY, V. E. SUOMI, F. W. TAYLOR, R. WOO, AND U. VON ZAHN 1980. Structure and circulation of the Venus atmosphere. *J. Geophys. Res.* **85,** 8007–8025.

SMREKAR, S. E. 1994. Evidence of active hotspots on Venus from analysis of *Magellan* gravity data. *Icarus* **112,** 2–26.

SILL, G. T. 1972. Sulfuric acid in the Venus clouds. *Comm. Lunar Planet. Lab.* **171,** 191–198.

TRAVIS, L. D. 1975. On the origin of ultraviolet contrasts on Venus. *J. Atmos. Sci.* **32,** 1190–1200.

TRAVIS, L. D., D. L. COFFEEN, J. E. HANSEN, K. KAWABATA, A. A. LACIS, W. A. LANE, S. S. LIMAYE, AND P. H. STONE 1979. Orbiter cloud photopolarimeter investigation. *Science* **203,** 781–785.

YOUNG, A. T. 1973. Are the clouds of Venus sulfuric acid? *Icarus* **18,** 564–582.

YOUNG, A. T. 1974. Venus Clouds: Structure and composition. *Science* **183,** 407–409.

YOUNG, A. T. 1975. The clouds of Venus. *J. Atmos. Sci.* **32,** 1125–1132.